Statistical characteristics of small-scale spatial and temporal electric field variability in the high-latitude ionosphere

E. D. P. Cousins[1] and S. G. Shepherd[1]

Received 17 November 2011; revised 6 January 2012; accepted 24 January 2012; published 16 March 2012.

[1] The statistical characteristics of small-scale spatial and temporal electric field variability in the high-latitude regions of Earth's ionosphere are investigated using 48 months of data from the Super Dual Auroral Radar Network (SuperDARN) radars in both hemispheres. Electric field fluctuations on spatial scales between 45 km and 450 km and on temporal scales between 2 min and 20 min are considered. It is found that both the distribution shapes and scale-size dependencies of the fluctuations are consistent with the expected properties of a turbulent flow. The observed spatial and temporal variability is influenced primarily by the magnitude of the shear or gradient in the background plasma drift and by season and solar cycle, suggesting plasma instabilities and gradients in the conductance as sources of the electric field variability. The relationship between spatial and temporal variability is investigated and it is found that the fluctuations are likely to be a mixture of convecting static and time-varying structures. It is also observed that the small-scale variability has statistical characteristics that are very similar in the two hemispheres. For practical purposes, although a stretched exponential function best matches the data, the distribution of observed electric field fluctuations can be approximated using an exponential function, enabling straightforward generation of nearly realistic random fluctuations.

Citation: Cousins, E. D. P., and S. G. Shepherd (2012), Statistical characteristics of small-scale spatial and temporal electric field variability in the high-latitude ionosphere, *J. Geophys. Res.*, *117*, A03317, doi:10.1029/2011JA017383.

1. Introduction

[2] In the Earth's ionosphere, plasma drifts in the high latitudes at *F* region altitudes (~150–800 km) are driven primarily by electric fields transmitted from the Earth's magnetosphere along magnetic field lines. These plasma drifts are often considered to have two components: a global convection pattern characterized by large spatial scales and variability (fluctuations) on smaller scales. The large-scale convection pattern is well-studied and is found to vary with the interplanetary magnetic field (IMF), solar wind velocity (V_{sw}), and the Earth's season or dipole tilt angle, among other parameters [e.g., *Weimer*, 2005; *Pettigrew et al.*, 2010]. Small-scale variability, defined here as fluctuations in the plasma drift electric field (and velocity) on spatial and temporal scales small compared to those of the global convection pattern, remains the subject of much investigation. This variability impacts the predictive ability of statistical models and can contribute to the total energy deposited in the atmosphere through Joule heating and mechanical energy transfer. The amount of energy contributed by small-scale electric field variability has been estimated in previous studies, but a possible anti-correlation between conductivity and small-scale variability makes such estimates difficult [e.g., *Cosgrove and Codrescu*, 2009; *Cosgrove et al.*, 2011; *Matsuo and Richmond*, 2008; *Johnson and Heelis*, 2005; *Deng et al.*, 2009].

[3] A number of theories exist regarding the nature and source of small-scale electric field variations, but no unified picture has emerged. Small-scale variations in the electric field are generally considered to be intermittently turbulent [e.g., *Kintner*, 1976; *Tam et al.*, 2005; *Golovchanskaya et al.*, 2006; *Abel et al.*, 2007, 2009; *Parkinson*, 2008] and to originate outside the ionosphere [e.g., *Gurnett et al.*, 1984; *Weimer et al.*, 1985]. Regarding the source of electric field variability, some theories associate the turbulence with structures of magnetospheric origin [e.g., *Ishii et al.*, 1992; *Golovchanskaya et al.*, 2006], driven by shear flow instabilities, for example. Others relate the turbulence in the ionosphere directly to turbulence in the solar wind [e.g., *Parkinson*, 2006; *Abel et al.*, 2009]. Regarding the spatial versus temporal nature of electric field variability, it has been postulated that the variability observed is primarily due to static, spatial structures at mesoscale lengths (~10–100 km and larger) and temporal variations at smaller scale lengths (~1–10 s and smaller) [e.g., *Knudsen et al.*, 1990; *Ishii et al.*, 1992; *Earle and Kelley*, 1993]. The assumption of static, spatial structures is often used to relate observed temporal variability to spatial variability [e.g., *Kintner*, 1976; *Weimer et al.*, 1985; *Golovchanskaya et al.*, 2006].

[4] With the aim of characterizing the turbulent behavior and identifying the origin of the turbulence, the scaling

[1]Thayer School of Engineering, Dartmouth College, Hanover, New Hampshire, USA.

0148-0227/12/2011JA017383

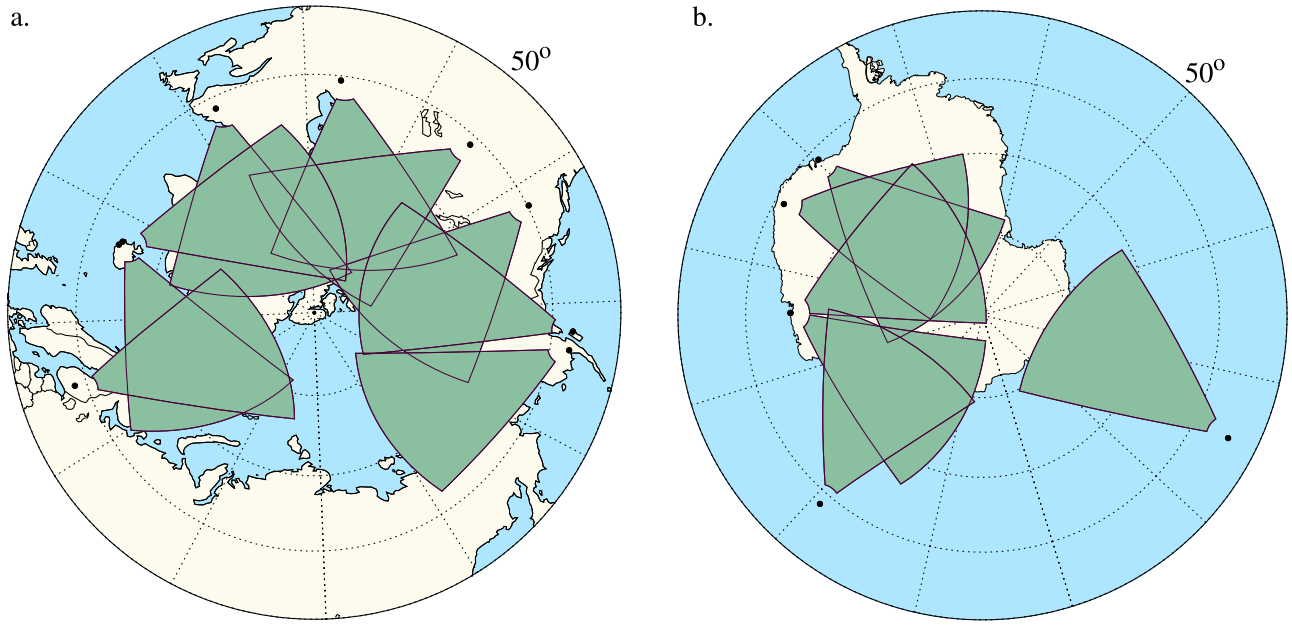

Figure 1. Map showing the locations (dots) and FOVs (shaded triangles) of (a) Northern and (b) Southern Hemisphere radars from which data for this study were obtained. The maps are plotted in geomagnetic coordinates.

properties of electric field (or equivalently, velocity) fluctuations have been the subject of many studies [e.g., *Kintner*, 1976; *Weimer et al.*, 1985; *Ishii et al.*, 1992; *Earle and Kelley*, 1993; *Heppner et al.*, 1993; *Tam et al.*, 2005; *Golovchanskaya et al.*, 2006; *Parkinson*, 2006; *Abel et al.*, 2007]. To estimate the contribution to the total electric field in the ionosphere and to the amount of energy input to the atmosphere, several statistical studies have also investigated the absolute magnitudes of small-scale electric field variability observed in the ionosphere [*Heppner et al.*, 1993; *Johnson and Heelis*, 2005; *Golovchanskaya et al.*, 2006; *Golovchanskaya*, 2007; *Matsuo and Richmond*, 2008]. These statistical studies were all based on data from the Dynamics Explorer (DE) 2 spacecraft, which operated for ~1.5 years (August, 1981 to February, 1983) during the declining phase of solar cycle 21.

[5] This paper seeks to characterize the statistical properties of small-scale spatial and temporal variability observed by the Super Dual Auroral Radar Network (SuperDARN) high-frequency (HF) radars in order to better understand the nature and possible drivers of electric field variability in the ionosphere, thereby enabling improved representation of this small-scale component in empirical or statistical models of ionospheric convection electric fields.

[6] Section 2 describes the method used to calculate small-scale electric field variability, section 3 describes the statistical characteristics of this small-scale variability and section 4 discusses possible implications of the results in context of previous studies.

2. Technique

[7] We first describe the selection of velocity data, the technique of calculating small-scale variability, and the selection of other geophysical and interplanetary data for organizing the variability data.

2.1. Velocity Data

[8] Velocity data are obtained from the SuperDARN HF coherent backscatter radars located in the high-latitude regions of both hemispheres. These radars provide measurements of the line-of-sight (LOS) component of the bulk $\mathbf{E} \times \mathbf{B}$ drift of *F*-region ionospheric plasma in the regions sampled by their fields of view (FOVs). All the radars included in this study transmit along 16 (electronically steered) beams within ~50° FOVs. In the typical radar operating mode (the only mode used in this study), the velocity data have a spatial resolution of 45 km in the LOS direction and the entire FOV is sampled once every 2 min. Because the velocity determination relies on Doppler shift information, velocities above a maximum magnitude of ~2000 m/s (dependent on the operating frequency) are aliased, limiting the range of velocity fluctuation magnitudes that can be accurately measured.

[9] For this study, 48 months of data (8 months per year) are used from 1999–2004, encompassing the maximum of solar cycle 23. In the Northern Hemisphere, data from February, April, May, June, July, August, October and December are included from each year, while in the Southern Hemisphere, January, February, April, June, August, October, November and December are included. This selection results in a more equal distribution of data across seasons, because generally less backscatter is observed during summer months [cf. *Ruohoniemi and Greenwald*, 1997]. During the years considered in this study, 6–9 radars in the Northern Hemisphere and 4–7 radars in the Southern Hemisphere were operational. The locations of these radars and their FOVs are shown in Figure 1. The data coverage

from these radars spans all local times and ~65°–90° geomagnetic latitude in both hemispheres.

[10] Several criteria are imposed on the data to ensure that only consistent and high-quality measurements from the *F*-region ionosphere are included in this study. SuperDARN radars run a variety of modes, sometimes sweeping in frequency or dwelling on a particular beam with higher time resolution. In order to ensure that all velocity measurements have the same spatial and temporal resolution, these special modes are excluded and only data from the normal 2-min operating mode are included.

[11] In these data, there are three primary sources of contamination: uncertainty resulting from the measurement technique, radar backscatter from the E-region ionosphere (below ~150 km altitude) and backscatter from the ground or sea (ground-scatter). To eliminate data likely to have a high degree of uncertainty, values are only included if the backscatter power (signal-to-noise ratio, SNR) is greater than 3 dB and if the error associated with the velocity determination is less than 150 m/s. This velocity error is based on the error in fitting the signal autocorrelation function to a functional form. To exclude the majority of E-region echoes, data from ranges <765 km from each radar (range-gate 13 or less) are not used. This threshold is based on the results of *Makarevich* [2010] who analyzed E-region echoes in all SuperDARN radars over a three year time period.

[12] Ground-scatter can be a serious problem in the radar data and inclusion of such echoes could lead to an overestimation of electric field variability. As an initial step, data flagged as ground-scatter by the standard SuperDARN data processing routines are excluded. This ground-scatter identification uses probabilistic criteria for the velocity, power and spectral width, based on a statistical study by *Baker et al.* [1988]. Because some ground-scatter is not identified (and is therefore classified as ionospheric scatter), an additional ground-scatter removal procedure is implemented as follows. Considering data from all range-gates (>13) from a given beam, the "*k*-means clustering algorithm" is applied to the velocity and position data. (*k*-means clustering is a standard data classification technique used to sort multidimensional data into classes [e.g., *MacQueen*, 1967].) The data are sorted by the algorithm into two classes, organized by velocity and position. If one class is identified whose centroid has velocity magnitude <100 m/s and the standard deviation of all the velocity data in that class is <100 m/s, the points in that class are considered to be ground-scatter and excluded. This ground-scatter removal is more drastic than the standard technique and as a result, more ionospheric scatter is classified as ground-scatter and excluded. However, the impact of including ground-scatter in a variability calculation (which would often create apparently large variability) is considered to be worse than the impact of excluding patches of low-velocity ionospheric data (which would generally have low variability).

2.2. Small-Scale Variability Calculation

[13] From the filtered velocity data set described in section 2.1, small-scale variability is measured at all locations/times with data available. Measuring the small-scale variability in a given location involves three steps: first, all velocity fluctuations about the location are measured; next, fluctuations that are likely to be noise are excluded; and finally, one fluctuation is randomly selected.

[14] For all available locations, spatial and temporal velocity fluctuations (differences) are calculated about the point (r, t), with fluctuations defined as $\Delta v_r(\Delta r) = v_{los}(r + \Delta r, t) - v_{los}(r, t)$ and $\Delta v_t(\Delta t) = v_{los}(r, t + \Delta t) - v_{los}(r, t)$. These fluctuations are illustrated in Figure 2. $\Delta v_r(\Delta r)$ is calculated for $\Delta r = \pm 45$ km, ± 90 km, ± 135 km, … ± 450 km (in the LOS direction), i.e., all range-gates up to ± 10 away from the selected point. $\Delta v_t(\Delta t)$ is calculated for $\Delta t = \pm 2$ min, ± 4 min, ± 6 min, … ± 20 mins, i.e., all consecutive scans up to 10 scans before and after the selected time. Up to 20 fluctuations are measured (± 10 increments) in both the spatial and temporal domain, but typically there are fewer than 20 filtered velocity data points in the vicinity. (Note that the upper scale sizes of 450 km and 20 mins are selected to exclude the effect of the large-scale convection pattern, based on the results of previous studies on velocity fluctuations in SuperDARN data. *Abel et al.* [2006] found that at scales of ~600–1000 km, velocity fluctuations were impacted by the large-scale convection pattern, and *Parkinson* [2008] found that variations on scales >34 min were probably influenced by large-scale convection.)

[15] Conditioning of the fluctuations is performed to reduce the impact of noise or aliasing from the velocity measurement technique. Fluctuations greater than $\sim 3\sigma$ (1200 m/s) are not included, where σ is the standard deviation of the unconditioned fluctuations. Similar conditioning was used by *Abel et al.* [2007]. In addition, a point (r, t) is only included if there are at least 7 filtered velocity data points out of the 20 possible adjacent points. These points are statistically unlikely to be noise. Note that because spatial and temporal fluctuations are calculated and conditioned independently, not all points have both spatial and temporal fluctuation measurements available, i.e., only spatial or only temporal fluctuations might have been measured at a given point.

[16] Once the fluctuations are calculated and conditioned, for every available location one Δv_r and one Δv_t value are randomly selected out of the up to 20 values in each domain (space and time) and these values are defined as the spatial and temporal variability at that location. This random selection is performed simply for the purpose of unbiased data reduction. Variability values are tabulated for each location containing filtered data, using all available beams from all available radars during the time period of the study. The result is a total of ~35 million spatial variability values from the Southern Hemisphere and ~70 million from the Northern Hemisphere, with similar numbers for temporal variability values. For analysis, each of these variability values is associated with its time, its location in Altitude Adjusted Corrected Geomagnetic (AACGM) coordinates and the magnetic azimuth angle of its LOS vector. Additionally, for each location, the median values of the velocity, power (SNR), and spectral width of the up to 40 adjacent points (± 10 range and time increments) are calculated. The spectral width values are derived from a functional fit to the power decay of the lags in the autocorrelation function.

[17] It should be noted that measurements from one position in the radar FOV (a particular beam/range-gate) but from separate times are actually separated in space also. This spatial separation exists because the ground-based radars

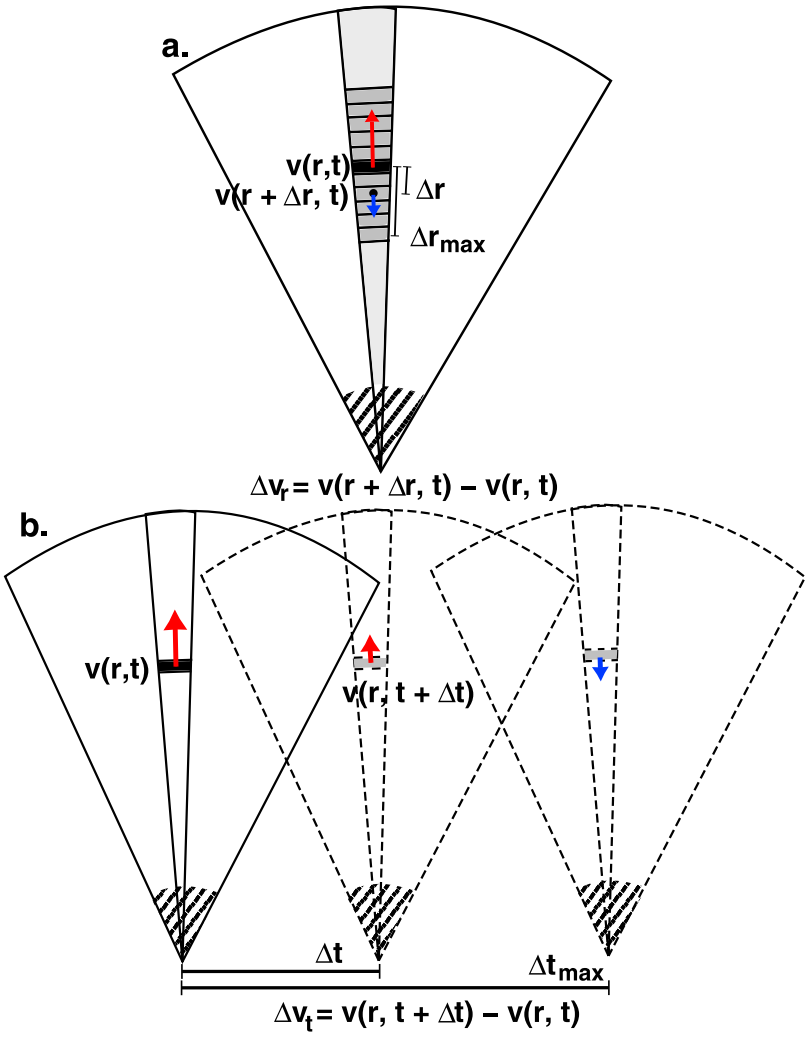

Figure 2. Diagram of a radar FOV illustrating how (a) spatial and (b) temporal velocity fluctuations are measured. Dark gray in Figure 2a indicates the area along a beam within $\pm\Delta r_{max}$ (450 km) of the point (r, t), shaded black. The dashed FOVs represent data taken at a later (or earlier) time. Lines are not drawn to scale.

travel in local time with the rotation of the Earth. As a result, the LOS directions of the radars rotate with respect to fixed Magnetic Local Time (MLT), such that a constant velocity vector would appear to vary with time. On small timescales (such as the ≤20 mins considered here), this variation is small (ranging from 0–10%, with the largest relative changes occurring in the smallest LOS velocities over the longest time increment) and can be neglected. Furthermore, because of the motion of the radars in local time, the 'temporal' variability calculated from the radar data includes a mixture of space and time variations. In the latitude range covered by the data (∼65–90°), the distance traveled by the scattering volume during the longest time increment (20 mins) is ∼0–250 km. Thus, the contribution of spatial variability to 'temporal' variability is expected to range from negligible at the highest latitudes to non-negligible near 65°. Such a mixture of spatial and temporal domains is a common feature of all studies of ionospheric data obtained from a single ground-, rocket- or satellite- based instrument. The impact of this mixing of domains will be discussed further in section 4.

2.3. Sorting Data

[18] In order to investigate possible drivers of ionospheric electric field variability, numerous interplanetary and geomagnetic parameters are used to sort the variability data. The selected parameters are chosen because they have been previously found to impact either large-scale or small-scale ionospheric plasma flows.

[19] Interplanetary magnetic field (IMF) and solar wind velocity and density information is obtained from one-minute resolution OMNI data from the CDAWeb database. The OMNI data set uses multispacecraft measurements of the interplanetary parameters that are lagged to the subsolar point on the Earth's bow shock [*King and Papitashvili*, 2005]. For this study, each variability value is tagged with the values of the interplanetary parameters averaged over the 60 min prior to the time of measurement. Note that while some studies found that averaging solar wind conditions over several hours with exponential weighting of the most recent hours was best at predicting

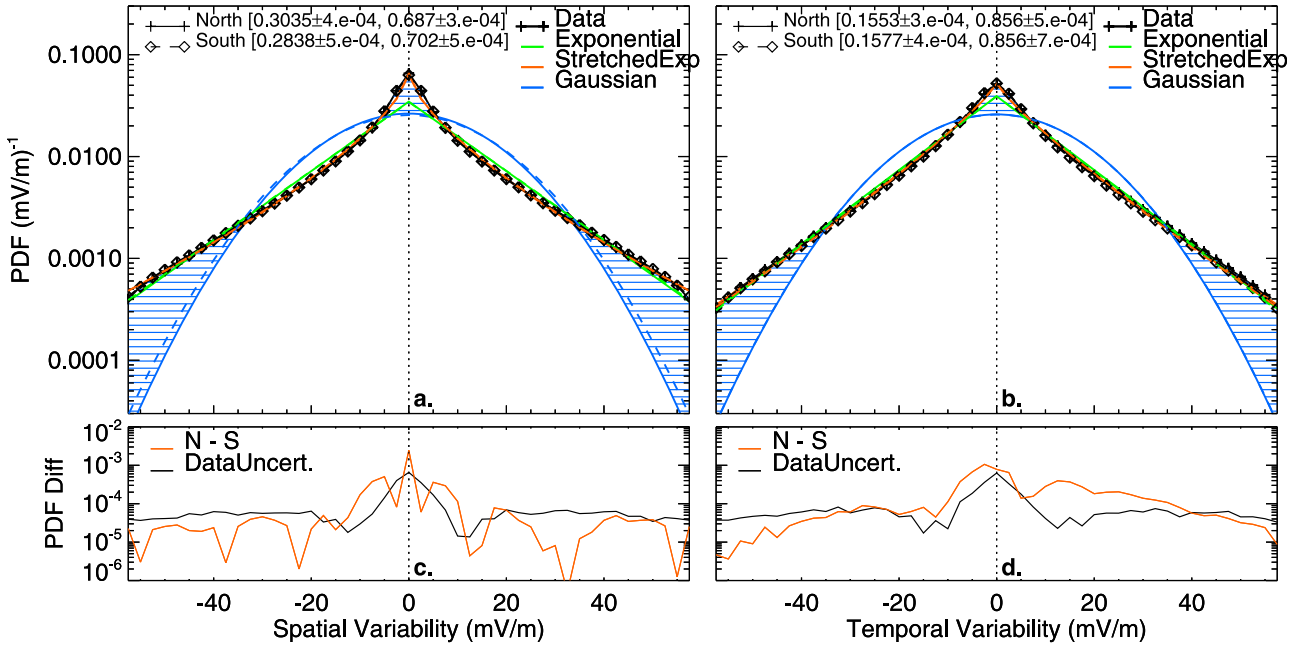

Figure 3. PDFs of (a) spatial and (b) temporal electric field fluctuations in the Northern (solid lines) and Southern (dashed lines) hemispheres. Colored lines show the best-fit exponential, stretched exponential, and Gaussian distributions. The coefficients of the best-fit stretched exponential distributions are given at top left of Figures 3a and 3b. The uncertainty in the PDFs and the difference between Northern and Southern PDFs are shown for (c) spatial and (d) temporal fluctuations, respectively.

many large-scale ionospheric parameters [*Wygant et al.*, 1983; *Newell et al.*, 2007] and another found that 45-min averages ending 10-min prior to the current observation was best [*Weimer*, 2005], several other variability studies [e.g., *Golovchanskaya et al.*, 2006; *Matsuo and Richmond*, 2008] use 60-min averages, as we do in this study.

[20] Variability values are also tagged with the instantaneous planetary *Kp* index (related to the maximum deviation of the geomagnetic field from its quiet time value) and the instantaneous Auroral Electrojet index AE (a measure of the deviation of the horizontal component of the geomagnetic field in the auroral region from its quiet time value). Values of the geomagnetic indices *Kp* and AE are obtained from the National Geophysical Data Center (NGDC) and the World Data Center for Geomagnetism, Kyoto, respectively. Note that the magnetometer measurements from which these indices are derived are all made in the Northern Hemisphere.

[21] Finally, the instantaneous dipole tilt angle is calculated for all variability measurements. This angle is defined as the magnitude of the angle between the Earth's best-fit magnetic dipole axis and the Geocentric Solar Magnetospheric (GSM) y-z plane. The sign is set such that positive and negative corresponds to sunlit and dark conditions, respectively, so that the dipole tilt values have opposite signs in the Northern and Southern hemispheres. The geomagnetic field model used in the calculation of the tilt angle is the International Geomagnetic Reference Field (IGRF-11).

3. Results

[22] Using the variability data described in section 2, we investigate the general distributions of the observed electric field fluctuations, the scale dependence of the fluctuations as well as various other dependencies of the average magnitudes and distributions of variability. Note that the analysis in this study is performed using electric field fluctuations derived from the SuperDARN LOS velocity measurements. This is possible because in the *F*-region, **V** and **E** are directly related to each other and by finding the value of the geomagnetic field at the locations of the velocity vectors, the data set can be converted from velocity to electric field values using the relation $\mathbf{E} = -\mathbf{V} \times \mathbf{B}$. This calculation is performed using magnetic field values from the IGRF model. Performing the analysis in terms of velocity or electric field gives very similar results (other than a scale factor of ~0.5 G in the variability magnitudes). Differences between the Northern and Southern Hemisphere, however, tend to be smaller in the electric field data than velocity data because differences in the magnitude of the geomagnetic field are taken into account.

3.1. Variability Distributions

[23] An important characteristic of variability is the relative distribution of fluctuation magnitudes. From the entire variability data set described in section 2.2, probability density functions (PDFs) of the electric field fluctuations are calculated independently for the Northern and Southern hemispheres for both spatial and temporal variability. Figures 3a and 3b show normalized PDFs for the Northern Hemisphere in solid lines, Southern Hemisphere in dashed lines, with colored lines representing several best-fit standard distribution functions: exponential, stretched exponential and Gaussian. The PDFs are only defined over the domain of the fluctuation data (−60 mV/m to 60 mV/m), which is set by the 3σ conditioning described in section 2.2. The statistical uncertainty (5th to 95th percentile interval) in

Table 1. Comparing the Use of the Exponential, Stretched Exponential, and Gaussian Distribution Functions to Represent the Spatial (S) and Temporal (T) Velocity Fluctuation PDFs From the Northern (N) and Southern (S) Hemispheres[a]

	Average (mV/m)		SD (mV/m)		RMS Fit Error		Total Error		μ (mV/m)		σ (mV/m)		λ (m/mV)		m	
	N	S	N	S	N	S	N	S	N	S	N	S	N	S	N	S
								Data								
S	10.1	10.3	11.3	11.7												
T	10.6	10.5	11.2	11.3												
								Exponential								
S	10.5	10.6	10.7	10.7	1.4e-2	1.4e-2	0.23	0.23	12.7	12.8	-	-	-	-	-	-
T	10.7	10.5	10.6	10.4	6.9e-3	7.5e-3	0.13	0.14	12.0	11.9	-	-	-	-	-	-
								Stretched Exponential								
S	9.9	10.0	11.1	11.1	3.8e-3	4.0e-3	0.06	0.06	-	-	-	-	0.304	0.284	0.688	0.702
T	10.4	10.3	10.7	10.6	2.4e-3	2.7e-3	0.04	0.05	-	-	-	-	0.155	0.158	0.856	0.856
								Gaussian								
S	12.0	12.4	9.1	9.4	1.9e-2	1.9e-2	0.46	0.46	0.0	0.0	15.1	15.6	-	-	-	-
T	12.2	12.3	9.3	9.3	1.4e-2	1.5e-2	0.37	0.38	0.0	0.0	15.4	15.4	-	-	-	-

[a]The calculation of the average and standard deviation of the distributions is performed on the absolute magnitude of the fluctuations and is limited to the domain of the fluctuation data (0–60 mV/m). μ, σ, λ, and m are the fit parameters described in the text.

the PDFs is estimated using bootstrap resampling [e.g., *Efron and Tibshirani*, 1993] and is found to be less than 4×10^{-4} for all curves shown, ranging from a fraction of a percent for small fluctuations to a few percent for large fluctuations (in the tails). The sum of the two hemispheres' uncertainty values, as well as the difference between the PDFs in the two hemispheres is shown in Figures 3c and 3d.

[24] As seen in Figure 3, PDFs of temporal variability are not identical to the corresponding PDFs of spatial variability, which have slightly flatter tails (i.e., a slightly larger percentage of large fluctuations). The relationship between spatial and temporal variability will be discussed further in section 4.

[25] Comparing PDFs between hemispheres, it is evident that PDFs of Northern Hemisphere fluctuations are approximately the same as PDFs of Southern Hemisphere fluctuations, for both spatial and temporal variability. As shown in Figures 3c and 3d, the difference between hemispheres is roughly at the level of uncertainty for spatial fluctuations, while it is statistically significant (above the level of uncertainty) for a large range of temporal fluctuations. This difference could be due to true differences in the distributions of electric field fluctuations in the two hemispheres or due to differences in the velocity data set resulting from differences in ground-scatter or noise characteristics, but in either case the difference is very small. Despite this difference, the shapes of the curves are very similar and the difference between spatial and temporal variability is consistent between the two hemispheres.

[26] Three standard distribution functions are fit to the fluctuation PDFs (shown in Figure 3): the exponential and the more general stretched exponential, which are distributions commonly used to describe turbulent parameters [e.g., *Castaing et al.*, 1990; *Kailasnath et al.*, 1992; *Burlaga*, 1993], and the Gaussian distribution. The exponential distribution has probability given by equation (1), the stretched exponential has probability given by equation (2) and the Gaussian distribution has probability given by equation (3),

$$p(x) \propto e^{-|x|/\mu} \tag{1}$$

$$p(x) \propto e^{-\lambda|x|^m} \tag{2}$$

$$p(x) \propto e^{-\frac{(x-\mu)^2}{2\sigma^2}} \tag{3}$$

where x is the electric field fluctuation in mV/m. All the distribution functions are normalized to the domain of the fluctuation data (−60 mV/m to 60 mV/m). The parameter values of the best-fit distributions are given in Table 1.

[27] The shapes of the PDFs observed in this study are consistent with those of *Golovchanskaya and Kozelov* [2010], who fit stretched exponential curves to the PDFs of 0.5–15 km electric field fluctuations measured by the DE-2 spacecraft. The stretching exponent, m, of the PDFs was found to be 0.44 and 0.6 on closed and open field lines, respectively. For the smallest scale size (45 km) of SuperDARN electric field fluctuations observed in this study, m is found to be ∼0.5, within the same range.

[28] Table 1 also lists the averages and standard deviations given by the standard distributions, compared to the data's values, as well as the root mean square (RMS) average of the difference between the fit PDFs and the data PDFs and the total absolute difference between the fit and data PDFs. Both temporal and spatial PDFs are well-represented by a stretched exponential distribution, which is the closest fit out of the three functional forms. The exponential distribution also closely approximates the observed PDFs, although for spatial variability it underestimates the probability of very small fluctuations (<5 mV/m).

[29] It is important to note that, as seen in Figure 3, neither temporal nor spatial variability can be effectively represented by a Gaussian distribution. If a Gaussian distribution were used to represent the variability data, as is commonly done, the probability of small fluctuations (<5 mV/m) and of

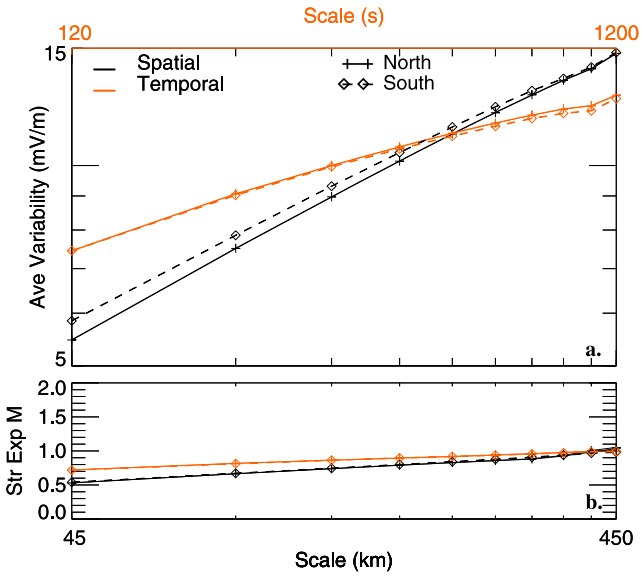

Figure 4. The (a) average magnitude and (b) best-fit stretching exponent of spatial (black curves) and temporal (red curves) electric field fluctuations in both hemispheres. Spatial fluctuations are sorted by spatial scale (given by bottom axis) and temporal fluctuations are sorted by temporal scale (given by top axis). Each curve is composed of two lines giving the statistical upper and lower bounds of the estimated value, although these lines are often not distinguishable due to very small errors. Note the logarithmic scales.

large fluctuations (>35 mV/m) would each be underestimated by ~10% (blue hatched regions in Figure 3). This Gaussian distribution would overestimate the average and underestimate the standard deviation of the fluctuation magnitudes by ~20% each. In comparison, an exponential distribution would overestimate the average by at most 5% and underestimate the standard deviation by at most 9%.

[30] Note that the PDFs considered here include data from all locations across the high-latitude and from all available time periods and are thus aggregate or average distributions. As discussed in section 3.3, the distributions are found to vary with, among other things, location and season, but the important properties such as the general shapes of the PDFs and the difference between spatial and temporal PDFs remain consistent.

3.2. Scale Dependence

[31] In turbulent flow, the power (and average magnitude) of velocity fluctuations is expected to have a power law-like dependence on scale size. Previous studies have observed such a dependence in ionospheric electric field and velocity fluctuations [e.g., *Heppner et al.*, 1993; *Parkinson*, 2006; *Abel et al.*, 2007]. In addition, the shape of the fluctuation PDF is expected to vary with scale size [*Kailasnath et al.*, 1992]. Note that the PDF's shown in Figure 3, and other figures throughout the paper, include electric field fluctuations from a mixture of scale sizes, ranging from 45–450 km in space and 2–20 mins in time. To investigate the dependence of spatial and temporal variability on scale size, we calculate the PDFs and the average magnitudes of fluctuations observed at varying scale sizes.

[32] Figure 4a shows the average magnitudes of spatial and temporal electric field fluctuations sorted by spatial and temporal scale size, given on the bottom and top horizontal axes, respectively. Sorting by scale size reveals that both spatial and temporal fluctuation magnitudes increase with increasing scale size, with similar behaviors (though not exactly the same values) in both hemispheres. Both spatial and temporal variability magnitudes approximately follow a power law, but spatial variability better fits such a dependence.

[33] Furthermore, for each of the possible scale sizes (45–450 km in 45 km increments and 2–20 mins in 2 min increments), PDFs are calculated from the electric field fluctuations observed at that scale size. Stretched exponential distributions are fit to the PDFs and the value of the stretching exponent, m, is plotted in Figure 4b. The parameter m is consistently larger for temporal than it is for spatial variability (by up to ~35%), but for both space and time, m increases monotonically from ~0.5 at the smallest scale to ~1.0 at the largest scale, with both hemispheres having very similar values. The implications of these observations are discussed in section 4.

3.3. Other Dependencies

[34] In order to identify factors which might influence small-scale electric field variability, the fluctuations are sorted by the observed gradient in the background plasma drift, by location, and by season and year. In addition, dependencies on a number of interplanetary and geomagnetic parameters, which are known to influence the large-scale convection of plasma, and the dependence on the spectral width of the velocity measurements are investigated.

[35] In this study, the single factor with the greatest impact on the observed spatial and temporal variability is the magnitude of the gradient in the local velocity. This gradient is defined as the slope of the best-fit linear trend to all the LOS velocity values within ±450 km in the LOS direction (for spatial measurements) or within ±20 mins (for temporal measurements) of a given point. Gradients are only calculated for linear fits with an R^2 value >0.7 and the spatial and temporal gradients are calculated separately. As shown in Figure 5, the distributions of the observed spatial and temporal gradients calculated in this manner have roughly exponential shapes. These distributions are approximately the same in both hemispheres and the overall averages of spatial and temporal gradient magnitudes are 0.38 mHz and 0.11 m/s^2, respectively.

[36] Note that if a shear exists in the background velocity field, it can be observed by LOS measurements as a velocity gradient. The magnitude of the resulting LOS velocity gradient will be at most half the magnitude of the velocity shear, depending on the angle between the LOS direction and the shear direction. This factor results from the projection of both the flow direction and the perpendicular (shear) direction onto the LOS direction. Any true gradients in the

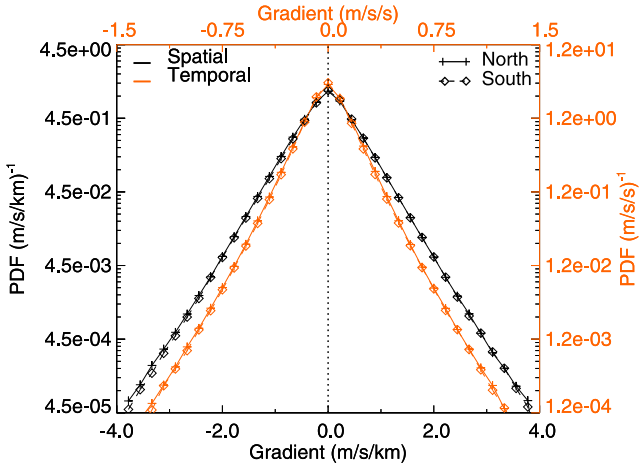

Figure 5. PDFs of spatial gradients (according to bottom and left axes) and temporal gradients (according to top and right axes) in the Northern (solid lines) and Southern (dashed lines) hemispheres.

background velocity can obviously also contribute to the observed gradient in the LOS direction.

[37] Figure 6a shows the average magnitude of fluctuations from both hemispheres, sorted by the magnitude of the local velocity gradient. Spatial and temporal fluctuations are sorted by the gradient of velocities in space and time, shown along the bottom and top horizontal axes, respectively. Note that the curves shown in Figure 6 only include locations with at least 15 adjacent data points available out of the 20 possible points (±10 range or time steps), ensuring very accurate measurements of the gradients.

[38] The average spatial and temporal variability are clearly seen to increase non-linearly with increasing gradient, with both hemispheres following approximately the same curve. These results are consistent with those of *Johnson and Heelis* [2005], who, using DE-2 data, analyzed the root mean squared (RMS) magnitude of small-scale velocity variability on scales between 2 km and 128 km and observed that the magnitude of small-scale velocity variability increases significantly with increasing magnitude of background velocity gradient. Note that *Johnson and Heelis* [2005] only considered time periods with steady, southward IMF while this study shows similar results including all time periods.

[39] The magnitude of the local velocity gradient also has a significant influence on the shape of the electric field fluctuation PDFs. For both spatial and temporal PDFs, the distributions widen as the velocity gradient magnitude increases, consistent with the increasing average magnitude. Furthermore, as shown in Figure 6b, the value of the best-fit stretching exponent, m, increases with increasing velocity gradient. This trend indicates that the PDFs of both spatial and temporal electric field fluctuations become more Gaussian for larger gradients. (Note that a Gaussian distribution function has m = 2.)

[40] Although spatial variability is most strongly correlated with velocity gradients in space and temporal variability is most strongly correlated to velocity gradients in time, both spatial and temporal variability do show similar dependences (increasing magnitude and increasing m) on gradients in the other domain (time and space, respectively).

[41] It is interesting to note that the magnitude of observed velocity gradients tends to vary with the magnetic azimuth angle of the LOS look-direction. Velocity gradient magnitudes tend to decrease when looking near the meridional direction and increase when looking near the zonal direction. On average, velocity gradients observed within ±10° of 90° magnetic azimuth (zonal direction) are ~20% greater than those observed within ±10° of 0° (meridional direction). The electric field variability also varies with azimuth angle, likely a consequence of this trend. For LOS vectors oriented in the zonal direction, the average spatial variability magnitude is ~20% greater than it is for those oriented in the meridional direction. These findings are consistent with the sounding rocket case study of *Earle et al.* [1989], who found that plasma flow in the zonal direction (parallel to typical auroral arcs) was most likely to be sheared, and that large electric field variability was associated with the sheared flow. Note that the dependence of temporal variability on azimuth angle is confounded because, as will be discussed in section 4, 'temporal' variability measured in the zonal direction includes a mixture of temporal and spatial fluctuations.

[42] After velocity gradient, the factor with the most influence on the observed variability is its location in magnetic coordinates. Note, however, that the magnitude of the velocity gradient also tends to vary with location, such that the location dependence of the variability described here appears to be determined in large part by the spatial distribution of velocity gradients.

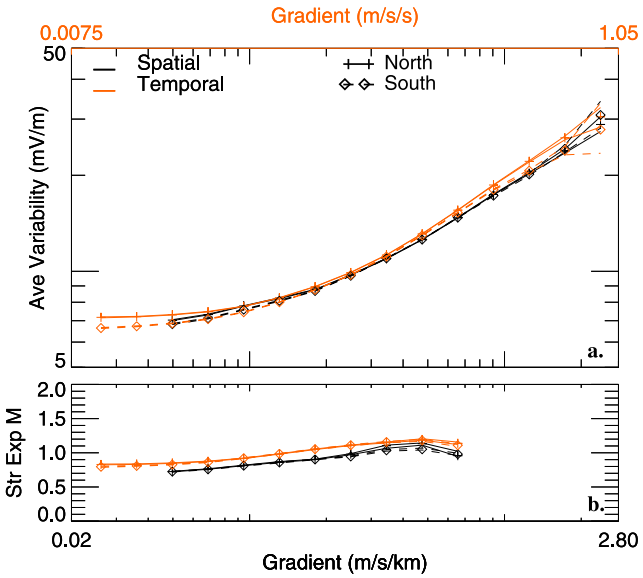

Figure 6. The (a) average magnitude and (b) best-fit stretching exponent of spatial (black curves) and temporal (red curves) electric field fluctuations in both hemispheres. Spatial fluctuations are sorted by spatial velocity gradient (given by bottom axis) and temporal fluctuations are sorted by temporal velocity gradient (given by top axis). Each curve is composed of two lines giving the statistical upper and lower bounds of the estimated value. Note the logarithmic scales.

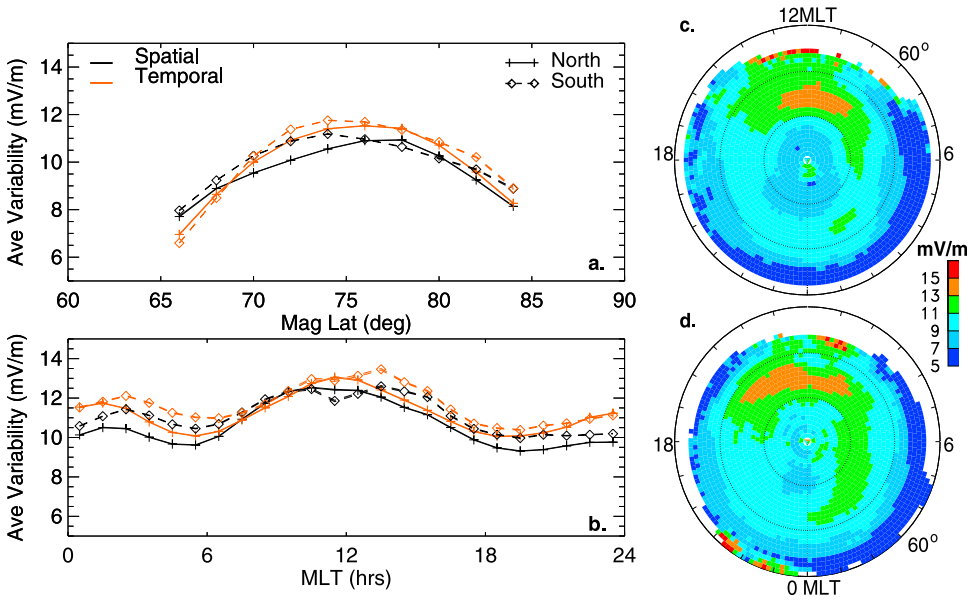

Figure 7. Average magnitude of spatial (black curves) and temporal (red curves) electric field fluctuations from both hemispheres, sorted by (a) magnetic latitude and (b) MLT. Each curve is composed of two lines giving the statistical upper and lower bounds of the estimated value. Maps of average spatial variability magnitudes in the (c) Northern and (d) Southern hemispheres.

[43] Sorting the variability data by its location in magnetic coordinates, it is found that the average magnitudes of spatial and temporal electric field fluctuations vary significantly with magnetic latitude and magnetic local time (MLT). Figure 7a shows the average magnitudes of all fluctuations, sorted into 2-degree bins of magnetic latitude. Figure 7b shows the averages of data between 70° and 80° latitude, sorted into 1-hour bins of MLT. All curves include two lines indicating upper and lower bounds on the estimate of the average, given by the 5% and 95% quantiles of the value of the average (from bootstrap resamples). This uncertainty is found to be always less than 0.1 mV/m.

[44] As shown in Figure 7a, both temporal and spatial variability magnitudes in the two hemispheres peak in the auroral zone (~70°−80°). In the Southern Hemisphere, the variability magnitude peaks at a slightly (~4°) lower latitude than in the Northern Hemisphere. Note that these latitude profiles are not expected to be controlled by counting statistics, as the amount of data has a different latitude profile, peaking at ~72° magnetic latitude in both hemispheres and falling off toward the poles. Considering the dependence on local time, it is observed that both temporal and spatial variability magnitudes in the two hemispheres peak on the dayside near noon MLT (see Figure 7b). In both hemispheres, variability averages are larger in the post-midnight/dawn sector than in the pre-midnight/dusk sector, although this feature is more pronounced in the Southern Hemisphere. In the Southern Hemisphere, the variability observed between 0–6 MLT is on average 13% larger than that observed between 18–24 MLT, while in the Northern Hemisphere this difference is just 5%. These latitude and local time features can be seen in maps of average spatial variability shown in Figures 7c and 7d for the Northern and Southern hemispheres, respectively. These maps are similar to those given by *Heppner et al.* [1993] and *Matsuo and Richmond* [2008], although those studies did not separate data from the two hemispheres.

[45] Previous studies have also identified a significant seasonal dependence in the magnitudes of small-scale electric field variability in DE-2 data [e.g., *Matsuo and Richmond*, 2008; *Golovchanskaya*, 2007]. To investigate any season or solar cycle dependence in the small-scale variability observed in SuperDARN data, Figure 8 shows 3-month averages of spatial and temporal electric field variability from between 70°

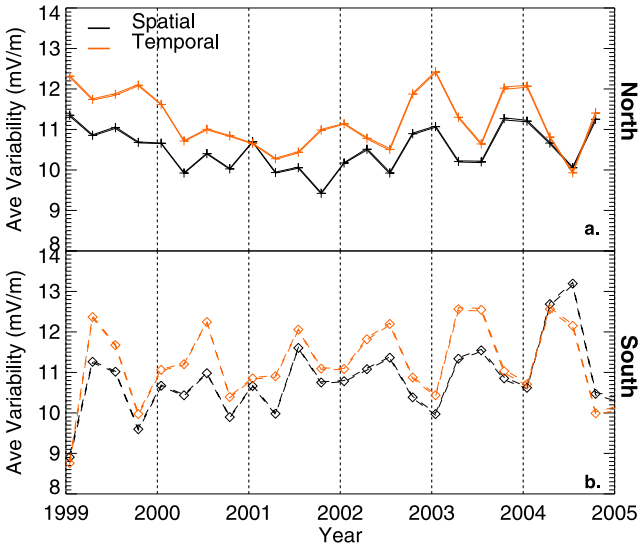

Figure 8. The average magnitude of spatial and temporal electric field fluctuations in the (a) Northern and (b) Southern hemispheres, sorted by date. Each curve is composed of two lines giving the statistical upper and lower bounds of the estimated value.

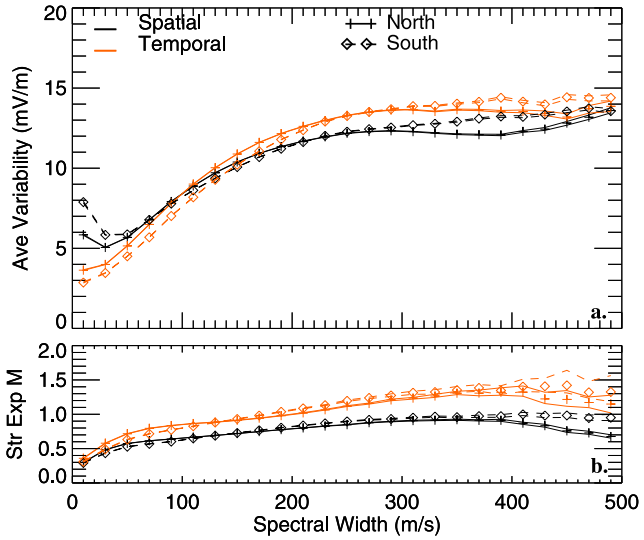

Figure 9. The (a) average magnitude and (b) best-fit stretching exponent of spatial (black curves) and temporal (red curves) electric field fluctuations in both hemispheres, sorted by spectral width. Each curve is composed of two lines giving the statistical upper and lower bounds of the estimated value.

and 80° latitude. The fluctuation magnitudes are found to vary significantly between different seasons and vary somewhat between different years. In the Southern Hemisphere, 'winter' spatial and temporal variability magnitudes are on average 27% and 28% higher, respectively, than corresponding 'summer' values. In the Northern Hemisphere the 'winter' to 'summer' differences are on average 11% and 20% in spatial and temporal variability, respectively. The value of the stretching exponent, m, is not found to vary significantly between seasons. Note that here we have defined 'winter' and 'summer' as times with dipole tilt angle $<-15°$ and $>15°$, respectively. Using true seasonal definitions (based on time-of-year) results in smaller winter-summer differences than using the dipole-tilt based definition. The trend of higher variability in the winter and lower variability in the summer is consistent with the findings of *Golovchanskaya* [2007] and *Matsuo and Richmond* [2008], although as will be discussed in section 4, the seasonal dependence observed in the DE-2 electric field variability is more drastic than that observed here.

[46] The Northern Hemisphere is observed to have a smaller seasonal dependence than that of the Southern Hemisphere, as seen in the smoother Northern Hemisphere curves in Figure 8. The source of this difference is not well-understood, although it is expected that one contributing factor is the smaller offset (19° versus 35° in the year 2000) between the magnetic and geographic poles in the Northern than Southern Hemisphere. Because of this difference, the sunlit regions of the geomagnetic high-latitude regions will be different between hemispheres for the same dipole tilt angle.

[47] In both hemispheres, the dependence appears weaker during the seasons near solar maximum (roughly 2000 through 2002) than away from solar maximum (see Figure 8). This solar cycle effect is especially strong in the Northern Hemisphere.

[48] Although the spatial and temporal variability are found to depend on the background velocity gradient, the location in magnetic coordinates and the season and solar cycle phase, several other dependencies are notably absent. The transverse magnitude $B_T \left(B_T = \sqrt{B_y^2 + B_z^2} \right)$ of the prevailing IMF, the solar wind velocity, and the current *Kp* and AE index all have no significant impact on the observed small-scale variability. Performing Pearson correlation analysis with 95% confidence bootstrap error analysis, no statistically significant correlation is observed in either hemisphere between spatial or temporal variability average magnitudes and any of these four parameters, with two exceptions. In the Northern Hemisphere, there is a small but statistically significant positive correlation between solar wind velocity and temporal variability magnitude. However, because neither Northern Hemisphere spatial variability nor Southern Hemisphere spatial or temporal variability show a dependence on solar wind velocity, it is likely that another hidden factor is the source of this correlation. The one other statistically significant correlation is a slight anti-correlation between *Kp* and spatial variability magnitudes in either hemisphere. Although this correlation is statistically significant, it is weak compared to the correlation between variability and velocity gradient, location, or season.

[49] The value of the IMF clock angle ($\tan^{-1}(B_y/B_z)$) significantly influences the distribution of variability in MLT and magnetic latitude but it is observed to have only a small influence on the overall average variability magnitude. A small but statistically significant anti-correlation is observed between the clock angle magnitude (0–180°) and the spatial or temporal variability magnitude in either hemisphere, with variability magnitudes being on average ~10% higher for northward than southward IMF.

[50] These results are generally consistent with those of previous studies. *Matsuo and Richmond* [2008] found that the average magnitude of small-scale electric field variability does not vary significantly with IMF clock angle. (No further sorting by other interplanetary or geomagnetic parameters was performed.) *Golovchanskaya et al.* [2002] observed a slight anti-correlation between activity level (measured by Dst or AE index) and the average magnitude of small-scale electric field fluctuations, while we observe no significant correlation with AE index but a slight anti-correlation between *Kp* and spatial variability magnitude.

[51] One other parameter that is correlated to small-scale electric field variability is the spectral width associated with the measured LOS velocity vectors, which is specific to the backscatter radar measurements used in this study and thus would not be seen in other studies. As shown in Figure 9, as the spectral width increases from 0 to ~200 m/s, the average magnitudes and the best-fit PDF stretching exponent, m, of both spatial and temporal variability in both hemispheres increase significantly. No further significant change in variability magnitude is observed as spectral width increases above 200 m/s. Temporal variability shows more variation with spectral width than does spatial variability, consistent with the fact that spectral width is primarily a temporal measurement. For very small spectral widths (<50 m/s),

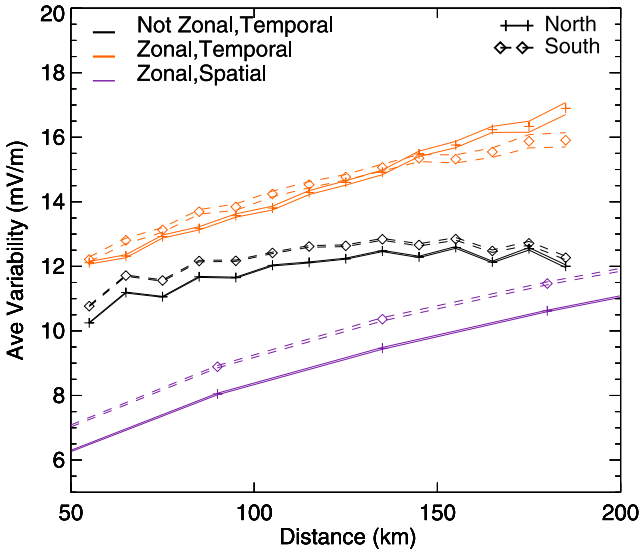

Figure 10. Average magnitudes of temporal electric field fluctuations observed in the zonal (red curve) or any other (black curve) direction, sorted by the distance traveled by the scattering volume. Average magnitudes of spatial electric field fluctuations observed in the zonal direction (purple curve) are sorted by spatial scale, according to the same axis. Each curve is composed of two lines giving the statistical upper and lower bounds of the estimated value.

both spatial and temporal variability averages are very small (~5 mV/m) and the electric field fluctuation PDFs are very narrow and non-Gaussian ($m \leq 0.5$).

4. Discussion

[52] Based the statistical characteristics and dependencies of small-scale electric field variability described in section 3, we consider the turbulent nature, the relationship between spatial and temporal fluctuations, and the important dependencies of the variability. The results are also compared to those of previous studies.

[53] The PDF shapes and the scale dependence of the observed spatial and temporal electric field fluctuations are consistent with the expected properties of a turbulent flow. *Barndorff-Nielsen* [1979] surveyed a number of observational studies of turbulence in neutral fluids and summarized that, in high Reynolds number turbulence, velocity differences (fluctuations) are expected to have probability density functions that are more peaked near zero and have a larger percentage of large values (heavier tails) than the Gaussian distribution, and have tails behaving like stretched exponentials. The PDFs observed in this study have all these properties. Furthermore, both spatial and temporal variability magnitudes approximately follow a power law dependence on scale size, consistent with the expected behavior of turbulent flow. Note, however, that temporal variability does not fit a power law as well as does spatial variability. This difference will be discussed later in this section. Finally, the changes in the shapes of the fluctuation PDFs with increasing scale size (as indicated by the changing stretching exponent m, shown in Figure 4b) are consistent with turbulent behavior. *Kailasnath et al.* [1992] fit stretched exponentials to PDFs of velocity fluctuations observed in a (neutral) turbulent fluid over a range of scales sizes. It was found that the stretching exponent, m, increased monotonically from ~0.5 in the smallest, 'dissipation,' scale size to ~2 in the largest, 'integral,' scale size. A similar behavior is observed in the ionospheric electric field fluctuations used in this study (see Figure 4b), but because the data set in this study covers a smaller range of scale sizes, m does not reach values much larger than 1. This interpretation of ionospheric small-scale variability as being turbulent is consistent with a number of previous studies that observed small-scale variability (on scales from 10's of meters to 100's of kilometers) in ionospheric electric and magnetic fields and considered it turbulent [e.g., *Kintner*, 1976; *Parkinson*, 2006; *Golovchanskaya et al.*, 2006; *Abel et al.*, 2007].

[54] An open question in the literature regards the nature of the relationship between spatial and temporal variability, i.e., do the observed temporal fluctuations result from electromagnetic waves or from convecting static structures. In an attempt to shed light on this topic, the spatial and temporal variability observed in this study are compared.

[55] One complication, however, is that 'temporal' electric field variability data in this study include a mixture of space and time variations, as discussed in section 2.2. To investigate the amount of spatial variations included in temporal data, the dependence of temporal electric field fluctuations on the distance traveled by the scattering volume is examined. The scattering volume is considered to be a specific region within the radar FOV (determined by the beam and range-gate where the given measurement was observed), and the distance it travels varies with the geographic latitude of the scattering volume and the length of time between measurements. If spatial variations contribute significantly to the temporal variability data, the average temporal variability magnitude would increase with increasing scattering volume movement. This dependence would exist due to the observed dependence of the spatial variability on spatial scale size.

[56] Figure 10 shows the average magnitudes of electric field fluctuations sorted by the distance traveled by the scattering volume. Because this distance is dependent on latitude and, as shown in section 3.3, spatial variability depends on latitude, the averages in Figure 10 are based only on data taken on the nightside (18–6 MLT) between 70°–80° magnetic latitude, where the dependence on latitude is the weakest (see Figures 7c and 7d). Temporal fluctuations measured in the zonal direction, (when the motion of the scattering volume is parallel to the LOS velocity vector) show a dependence on scattering volume movement. As expected, this dependence is similar to the dependence of spatial variability on spatial scale size (purple curve in Figure 10) and is likely due to the inclusion of spatial variations. For all other orientations (which account for 94% of all the data), however, no dependence is observed and the temporal variability data is expected to be in fact dominated by time variations.

[57] Having established that spatial and temporal variability data are primarily independent measurements of space and time variations (in all but the 6% of the LOS velocity vectors that are zonally oriented), it is meaningful to compare them. In general, as seen in section 3.1, spatial and temporal data have very similar behaviors and have similar magnitudes, with the biggest differences being that the

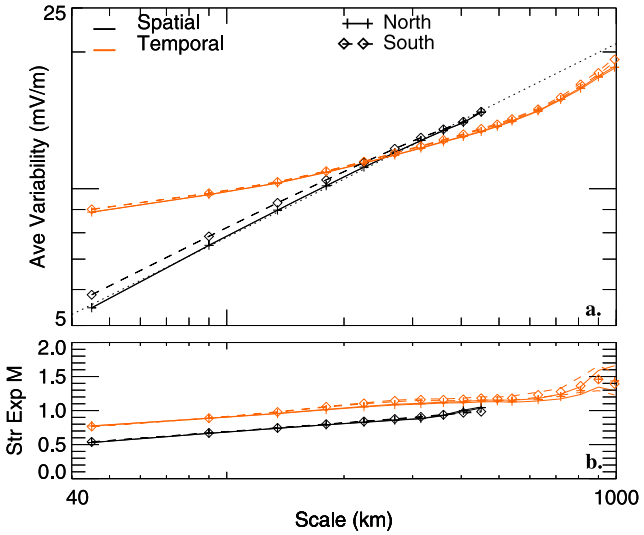

Figure 11. The (a) average magnitude and (b) best-fit stretching exponent of spatial (black curves) and temporal (red curves) electric field fluctuations in both hemispheres. Spatial fluctuations are sorted by spatial scale and temporal fluctuations are sorted by pseudo-spatial scale (see text). Each curve is composed of two lines giving the statistical upper and lower bounds of the estimated value. Note the logarithmic scales.

spatial fluctuation PDFs have slightly flatter tails (and therefore lower stretching exponent, m) than temporal PDFs and the average magnitudes of temporal fluctuations do not appear to fit a power law dependence on scale size as well as do spatial fluctuations.

[58] One likely cause of this similarity is that temporal variability is simply the result of convecting static structures (e.g., the Taylor hypothesis [*Taylor*, 1938]). In this case, temporal scales can be converted to pseudo-spatial scales based on the magnitude of the background, average drift velocity.

[59] As shown in Figure 11, both the average magnitude and the stretching exponent, m, of the PDFs of temporal fluctuations increase with increasing pseudo-spatial scale. The dependence on pseudo-spatial scale of m is approximately the same as the dependence of m for spatial variability on spatial scale. Also, for scales sizes >∼400 km, the average magnitudes of temporal fluctuations are similar to those of spatial fluctuations, consistent with the theory of convecting static structures. However, the temporal variability for small pseudo-spatial scales is much larger than the corresponding spatial variability at that spatial scale and the stretching exponent for temporal fluctuations is offset from that of spatial fluctuations. These differences persist even after selecting only times with large (>500 m/s, 25 mV/m) background drift velocities (when the Taylor hypothesis is more valid). Furthermore, considering all individual measurements when the pseudo-spatial scale of the temporal fluctuation matches the spatial scale of the spatial fluctuation, the correlation between the values of spatial and temporal fluctuations is less than 0.35 in both hemispheres.

[60] These results suggest that although convecting static structures likely contribute to the observed temporal fluctuations, this is probably not the only source of temporal variability. That the observed dependence of temporal variability on temporal scale size does not follow a power law as well as does spatial variability supports this theory and suggests that something other than just a turbulent cascade of energy to smaller scales is contributing to the observed temporal variability. The additional contribution could come from Alfvén wave activity. Note that, in investigating small-scale variability in DE-2 electric field data, *Heppner et al.* [1993] found evidence for Alfvén wave contributions at scales up to 2 km (the largest scale observed in that study).

[61] The observed small-scale electric field variability, regardless of its static or electromagnetic nature, appears to be significantly influenced by two primary factors: velocity gradients or shears and ionospheric conductance. The dependence of variability on the gradient in the background plasma drift is likely due to the development of instabilities (such as the Kelvin-Helmholtz instability) in regions of velocity shear, which can generate small-scale turbulence [e.g., *Keskinen et al.*, 1988; *Nishikawa et al.*, 1990]. (Note that, as discussed in section 3.3, velocity shears are observed as gradients in the LOS measurements used in this study.) Previous case studies using DE-2 data [*Basu et al.*, 1988] and sounding rocket data [*Earle et al.*, 1989] have also observed increased structure or variability in regions with large shears in the background velocity. This dependence on velocity shear is a likely source of the observed dependence of variability on azimuth angle (with larger variability in zonal drifts). It is also a possible source of the location dependence of variability, which peaks in the auroral zone latitudes and near noon MLT, regions which are also observed to have larger-than-average velocity shears or gradients.

[62] The seasonal and solar cycle dependence that is observed in the spatial and temporal variability data suggests that the magnitude of variability is influenced by the background ionospheric conductance, because season (or dipole tilt angle) controls how much of the polar cap is sunlit and the solar cycle influences the total solar irradiance, both of which impact ionospheric conductance. In summer or solar maximum conditions, the higher background conductance and smaller relative role of precipitation are expected to result in a smoother conductance pattern in the high-latitudes, a possible cause of the smaller electric field variability.

[63] Note that the seasonal/dipole tilt dependence observed in the SuperDARN electric field variability in this study is much weaker than the seasonal dependences observed in previous statistical studies. Using DE-2 data, previous studies found that the average magnitudes of electric field variations on scales from 3–500 km are 2–3 times larger in the winter than in the summer [*Golovchanskaya*, 2007; *Matsuo and Richmond*, 2008]. On the other hand, for the small-scale variability observed in this study, the winter variability averages are at most 1.28 times larger than summer variability averages. Several factors can contribute to this apparent inconsistency. First, SuperDARN measurements are made at lower altitude than the satellite measurements. The impact of this altitude difference is not fully understood, but one previous study noted a conductivity-related altitude dependence in the magnitudes of small-scale variability [*Weimer et al.*, 1985]. Second, a large portion of the SuperDARN data set comes from times near solar maximum while DE-2 data comes from the declining phase

of the solar cycle. During the declining phase, the seasonal dependence of variability observed in the SuperDARN data is larger than that observed during solar maximum. Third, the SuperDARN data set has complete MLT coverage during all seasons, while DE-2 local time coverage is dependent on season, with most solstice data coming from the dawn and dusk sectors and slightly more dayside data during the summer and slightly more nightside data during the winter. In the SuperDARN data set, selecting data from only these local times results in a larger seasonal dependence in variability than that observed over all local times. Finally, previous studies have reported that the seasonal dependence is stronger for higher geomagnetic latitudes (above 70° [*Golovchanskaya*, 2007] or 80° [*Heppner et al.*, 1993]). The SuperDARN data coverage used for this study drops off quickly above 75° and thus does not include much of this seasonal-dependent region and probably underestimates the overall average seasonal trend. These factors combined suggest that the SuperDARN variability data underestimates the average seasonal dependence and the DE-2 variability data overestimates the average seasonal dependence, explaining to some extent why studies using DE-2 data report a much larger seasonal dependence than this SuperDARN-based study.

[64] It is interesting that several factors which strongly influence large-scale convection appear to have little influence on small-scale electric field variability, particularly interplanetary parameters (IMF clock angle, IMF transverse magnitude, solar wind velocity and solar wind density) and the AE or *Kp* indices. These results are consistent with the results of *Golovchanskaya et al.* [2002] and *Matsuo and Richmond* [2008]. The lack of dependence on these parameters implies that dayside reconnection and geomagnetic activity are probably not significant drivers of small-scale electric field variability in the ionosphere.

[65] A correlation specific to SuperDARN observations is that between small-scale electric field variability and the spectral width associated with the Doppler velocity measurement. This correlation, which exists only for small spectral widths, confirms the results of *Ponomarenko and Waters* [2006] and *Ponomarenko et al.* [2007], who investigated the spectral characteristics of SuperDARN backscatter and inferred that for low values ($<\sim$150m/s), spectral width is likely controlled by small-scale velocity fluctuations.

[66] One final practical note concerns the problem of generating realistic electric field variability. Although out of the three distributions considered, the stretched exponential distribution best describes the observed fluctuations, generating random variables with such a distribution is not straightforward. An exponential distribution, however, can approximate the distribution of observed fluctuations (with much better accuracy than a Gaussian distribution) and random variables with this distribution are easily generated. This finding suggests that, in practice, an exponential distribution should be used to represent small-scale ionospheric electric field fluctuations.

5. Summary

[67] We investigate the properties of small-scale spatial and temporal electric field variability using 48 months of SuperDARN plasma drift data taken in the Northern and Southern hemispheres over six years. Considering fluctuations on spatial scales between 45 km and 450 km and on temporal scales between 2 min and 20 min, we calculate the PDFs of electric field fluctuations and determine the scale-size dependence of both the average variability magnitudes and the PDF shapes. These characteristics are found to be consistent with the expected behavior of turbulent flow. In addition, to investigate possible drivers of small-scale electric field variability, various dependencies of these fluctuations are examined. It is found that gradients or shears in the background plasma drift and season and solar cycle strongly influence small-scale variability, suggesting plasma instabilities and gradients in the conductance as likely sources. On the other hand, parameters associated with dayside reconnection or geomagnetic activity, such as IMF magnitude or clock angle and AE or *Kp* index, have little or no influence on the observed electric field variability. To investigate the static versus electromagnetic nature of the variability, we compare the observed spatial and temporal fluctuations. Although correlations between space and time variations are observed, differences in the behaviors of spatial and temporal variability suggest that temporal variability on 2–20 min scales is probably more than just convecting static structures. We also note that all the statistical characteristics of small-scale variability considered in this study are consistent between the two hemispheres and often the two hemispheres are nearly identical. Considering how the observed electric field variability might be reproduced in practice, it is found that an exponential distribution can both approximately represent the observed fluctuations and be easily implemented.

[68] **Acknowledgments.** Operation of the SuperDARN radars is supported by the national funding agencies of the United States, Canada, the United Kingdom, France, Japan, Italy, South Africa, and Australia. We gratefully acknowledge the CDAWeb for providing the high-resolution OMNI data, the WDC for Geomagnetism, Kyoto for providing the AE index and the National Geophysical Data Center for providing the KP index used in this study. This work was supported by NSF grants ATM-0836485 and ATM-0838356, and NASA grant NNX10AL97H.

[69] Robert Lysak thanks the reviewers for their assistance in evaluating this paper.

References

Abel, G. A., M. P. Freeman, and G. Chisham (2006), Spatial structure of ionospheric convection velocities in regions of open and closed magnetic field topology, *Geophys. Res. Lett.*, *33*, L24103, doi:10.1029/2006GL027919.

Abel, G. A., M. P. Freeman, G. Chisham, and N. W. Watkins (2007), Investigating turbulent structure of ionospheric plasma velocity using the Halley SuperDARN radar, *Nonlinear Processes Geophys.*, *14*(6), 799–809.

Abel, G. A., M. P. Freeman, and G. Chisham (2009), IMF clock angle control of multifractality in ionospheric velocity fluctuations, *Geophys. Res. Lett.*, *36*, L19102, doi:10.1029/2009GL040336.

Baker, K. B., R. A. Greenwald, J.-P. Villain, and S. Wing (1988), Spectral characteristics of high frequency (HF) backscatter from high-latitude ionospheric irregularities: Preliminary analysis of statistical properties, *Tech. Rep. RADC-TR-87-204*, Rome Air Dev. Cent., Griffis Air Force Base, N. Y.

Barndorff-Nielsen, O. (1979), Models for non-Gaussian variation, with applications to turbulence, *Proc. R. Soc. London, Ser. A*, *368*(1735), 501.

Basu, S., S. Basu, E. MacKenzie, P. F. Fougere, W. R. Coley, N. C. M. J. D. Winningham, M. Sugiura, W. B. Hanson, and W. R. Hoegy (1988), Simultaneous density and electric field fluctuation spectra associated with velocity shears in the auroral oval, *J. Geophys. Res.*, *93*, 115.

Burlaga, L. F. (1993), Intermittent turbulence in large-scale velocity fluctuations at 1 AU near solar maximum, *J. Geophys. Res.*, *98*, 17,467.

Castaing, B., Y. Gagne, and E. J. Hopfinger (1990), Velocity probability density functions of high Reynolds number turbulence, *Phys. D*, *46*, 177.

Cosgrove, R., M. McCready, R. Tsunoda, and A. Stromme (2011), The bias on the Joule heating estimate: Small-scale variability versus resolved-scale model uncertainty and the correlation of electric field and conductance, *J. Geophys. Res.*, *116*, A09320, doi:10.1029/2011JA016665.

Cosgrove, R. B., and M. V. Codrescu (2009), Electric field variability and model uncertainty: A classification of source terms in estimating the squared electric field from an electric field model, *J. Geophys. Res.*, *114*, A06301, doi:10.1029/2008JA013929.

Deng, Y., A. Maute, A. D. Richmond, and R. G. Roble (2009), Impact of electric field variability on Joule heating and thermospheric temperature and density, *Geophys. Res. Lett.*, *36*, L08105, doi:10.1029/2008GL036916.

Earle, G. D., and M. C. Kelley (1993), Spectral evidence for stirring scales and two-dimensional turbulence in the auroral ionosphere, *J. Geophys. Res.*, *98*, 11,543.

Earle, G. D., M. C. Kelley, and G. Ganguli (1989), Large velocity shears and associated electrostatic waves and turbulence in the auroral F region, *J. Geophys. Res.*, *94*, 15,321.

Efron, B., and R. J. Tibshirani (1993), *An Introduction to the Bootstrap*, CRC Press, Boca Raton, Fla.

Golovchanskaya, I. V. (2007), On the seasonal variation of electric and magnetic turbulence at high latitudes, *Geophys. Res. Lett.*, *34*, L13103, doi:10.1029/2007GL030125.

Golovchanskaya, I. V., and B. V. Kozelov (2010), On the origin of electric turbulence in the polar cap ionosphere, *J. Geophys. Res.*, *115*, A09321, doi:10.1029/2009JA014632.

Golovchanskaya, I. V., Y. P. Maltsev, and A. A. Ostapenko (2002), High-latitude irregularities of the magnetospheric electric field and their relation to solar wind and geomagnetic conditions, *J. Geophys. Res.*, *107*(A1), 1001, doi:10.1029/2001JA900097.

Golovchanskaya, I. V., A. A. Ostapenko, and B. V. Kozelov (2006), Relationship between the high-latitude electric and magnetic turbulence and the Birkeland field-aligned currents, *J. Geophys. Res.*, *111*, A12301, doi:10.1029/2006JA011835.

Gurnett, D., R. Huff, J. Menietti, J. Burch, J. Winningham, and S. Shawhan (1984), Correlated low-frequency electric and magnetic noise along the auroral field lines, *J. Geophys. Res.*, *89*(10), 8971–8985.

Heppner, J. P., M. C. Liebrecht, N. C. Maynard, and R. F. Pfaff (1993), High-latitude distributions of plasma waves and spatial irregularities from DE2 alternating current electric field observations, *J. Geophys. Res.*, *98*, 1629.

Ishii, M., M. Sugiura, T. Iyemori, and J. Slavin (1992), Correlation between magnetic and electric-field perturbations in the field-aligned current regions deduced from DE 2 observations, *J. Geophys. Res.*, *97*(A9), 13,877–13,887.

Johnson, E., and R. Heelis (2005), Characteristics of ion velocity structure at high latitudes during steady southward interplanetary magnetic field conditions, *J. Geophys. Res.*, *110*, A12301, doi:10.1029/2005JA011130.

Kailasnath, P., K. R. Sreenivasan, and G. Stolovitzky (1992), Probability density of velocity increments in turbulent flows, *Phys. Rev. Lett.*, *68*(18), 2766–2769.

Keskinen, M. J., H. G. Mitchell, J. A. Fedder, P. Satyanarayana, S. T. Zalesak, and J. D. Huba (1988), Nonlinear evolution of the Kelvin-Helmholtz instability in the high-latitude ionosphere, *J. Geophys. Res.*, *93*, 137.

King, J. H., and N. E. Papitashvili (2005), Solar wind spatial scales in and comparisons of hourly Wind and ACE plasma and magnetic field data, *J. Geophys. Res.*, *110*, A02104, doi:10.1029/2004JA010649.

Kintner, P. M., Jr. (1976), Observations of velocity shear driven plasma turbulence, *J. Geophys. Res.*, *81*, 5114.

Knudsen, D., M. Kelley, G. Earle, J. Vickrey, and M. Boehm (1990), Distinguishing Alfven waves from quasi-static field structures associated with the discrete aurora-sounding rocket and HILAT satellite measurements, *Geophys. Res. Lett.*, *17*(7), 921–924.

MacQueen, J. B. (1967), Some methods for classification and analysis of multivariate observations, in *Proceedings of the Fifth Berkeley Symposium on Mathematical Statistics and Probability*, vol. 1, edited by L. M. L. Cam and J. Neyman, pp. 281–297, Univ. of Calif. Press, Berkeley.

Makarevich, R. A. (2010), On the occurrence of high-velocity E-region echoes in SuperDARN observations, *J. Geophys. Res.*, *115*, A07302, doi:10.1029/2009JA014698.

Matsuo, T., and A. D. Richmond (2008), Effects of high-latitude ionospheric electric field variability on global thermospheric Joule heating and mechanical energy transfer rate, *J. Geophys. Res.*, *113*, A07309, doi:10.1029/2007JA012993.

Newell, P. T., T. Sotirelis, K. Liou, C. I. Meng, and F. J. Rich (2007), A nearly universal solar wind-magnetosphere coupling function inferred from 10 magnetospheric state variables, *J. Geophys. Res.*, *112*, A01206, doi:10.1029/2006JA012015.

Nishikawa, K.-I., G. Ganguli, Y. C. Lee, and P. J. Palmadesso (1990), Simulation of electrostatic turbulence due to sheared flows parallel and transverse to the magnetic field, *J. Geophys. Res.*, *95*, 1029.

Parkinson, M. L. (2006), Dynamical critical scaling of electric field fluctuations in the greater cusp and magnetotail implied by HF radar observations of F-region Doppler velocity, *Ann. Geophys.*, *24*(2), 689–705.

Parkinson, M. L. (2008), Complexity in the scaling of velocity fluctuations in the high-latitude F-region ionosphere, *Ann. Geophys.*, *26*(9), 2657–2672.

Pettigrew, E. D., S. G. Shepherd, and J. M. Ruohoniemi (2010), Climatological patterns of high-latitude convection in the Northern and Southern hemispheres: Dipole tilt dependencies and interhemispheric comparisons, *J. Geophys. Res.*, *115*, A07305, doi:10.1029/2009JA014956.

Ponomarenko, P. V., and C. L. Waters (2006), Spectral width of SuperDARN echoes: Measurement, use and physical interpretation, *Ann. Geophys.*, *24*, 115.

Ponomarenko, P. V., C. L. Waters, and F. W. Menk (2007), Factors determining spectral width of HF echoes from high latitudes, *Ann. Geophys.*, *25*, 675.

Ruohoniemi, J. M., and R. A. Greenwald (1997), Rates of scattering occurrence in routine HF radar observations during solar cycle maximum, *Radio Sci.*, *32*, 1051.

Tam, S., T. Chang, P. Kintner, and E. Klatt (2005), Intermittency analyses on the SIERRA measurements of the electric field fluctuations in the auroral zone, *Geophys. Res. Lett.*, *32*, L05109, doi:10.1029/2004GL021445.

Taylor, G. I. (1938), The spectrum of turbulence, *Proc. R. Soc. London, Ser. A*, *164*(919), 476–490.

Weimer, D., C. Goertz, D. Gurnett, N. Maynard, and J. Burch (1985), Auroral-zone electric-fields from DE-1 and DE-2 at magnetic conjunctions, *J. Geophys. Res.*, *90*(A8), 7479–7494.

Weimer, D. R. (2005), Improved ionospheric electrodynamic models and application to calculating Joule heating rates, *J. Geophys. Res.*, *110*, A05306, doi:10.1029/2004JA010884.

Wygant, J. R., R. B. Torbert, and F. S. Mozer (1983), Comparision of S3-3 polar cap potential drops with the interplanetary magnetic field and models of magnetopause reconnection, *J. Geophys. Res.*, *88*(A7), 5727.

E. D. P. Cousins and S. G. Shepherd, Thayer School of Engineering, Dartmouth College, Hanover, NH 03755, USA. (ellen.cousins@dartmouth.edu)